ChemComm

COMMUNICATION

View Article Online
View Journal

Cite this: DOI: 10.1039/d5cc06597f

Received 20th November 2025,
Accepted 5th January 2026

DOI: 10.1039/d5cc06597f

rsc.li/chemcomm

A pH-responsive iron/manganese bimetallic organic framework nanosystem for synergistic therapy of colon cancer

Siyuan Wang,[a] Shichen Zhang,[b] Xue Jia,[a] Xinran Yan,[a] Yixin Tang,[a] Mujie Kan,[a] Chang Liu*[c] and Caina Xu *[a]

A system loaded with MTO and encapsulated in SA achieved efficient drug delivery and tumor- microenvironment-triggered release. This release of MTO further exerted its chemotherapeutic effects and, in conjunction with ferroptosis, induced immunogenic cell death.

Colon cancer is one of the most common malignant tumours worldwide, ranking second in the number of deaths.[1] Due to the high recurrence rate of colorectal tumours and the low specificity and toxic side effects of available treatments, patients with advanced colon cancer often have a poor prognosis.[2] Therefore, the development of new anticancer strategies that can simultaneously target the tumour microenvironment and activate the body's immune system has become a key research direction.

Ferroptosis, a programmed cell death pathway accompanied by iron-mediated lipid peroxidation (LPO), has attracted much attention because of its great potential in anticancer therapy. During ferroptosis, depletion of glutathione (GSH) decreases glutathione peroxidase 4 (GPX4) activity and leads to impaired cellular antioxidant capacity. Under the catalysis of the Fenton/Fenton-like reaction mediated by metal ions such as Fe/Mn, reactive oxygen species (ROS) accumulate in large quantities, which in turn trigger the occurrence of lipid peroxidation and ultimately ferroptosis.[3] More critically, cancer cells undergoing ferroptosis are usually also undergoing immunogenic cell death (ICD), and the anticancer drug mitoxantrone (MTO) can not only inhibit tumour growth but also induce ICD to occur.[4] The ICD induces the release of damage-associated molecular pattern (DAMP), which is a key component in the development of cancer cells. ICD is characterized mainly by the exposure of calreticulin (CRT) and the release of high mobility group box 1 (HMGB1).[5] The ICD ultimately produces a powerful anti-tumour immune response. In order to overcome the delivery bottlenecks of traditional chemotherapy drugs, we use metal–organic framework (MOF) materials to load chemotherapy drugs and achieve the synergistic therapeutic effect of ferroptosis and ICD.

Based on the therapeutic synergy of involving ferroptosis with ICD and the excellent performance of MOFs, we designed a composite nano-delivery system, denoted as FMMS NPs, which had the anticancer drug MTO loaded into the porous structure of Fe/Mn bimetallic MOFs, followed by use of sodium alginate (SA) for surface modification (Fig. 1). The FMMS NPs decomposed in the acidic reducing conditions of the tumour microenvironment, releasing Fe and Mn ions. These ions could catalyse the generation of ROS *via* Fenton and Fenton-like reactions, and also catalyse the downregulation of GPX4, triggering the occurrence of LPO and ultimately ferroptosis. And, ferroptosis effectively induced the occurrence of ICD in tumour cells.[6] Furthermore the loaded MTO could be released at the tumour sites to directly kill tumour cells. MTO could effectively induce tumour cells to undergo ICD. The multifunctional nano-delivery system comprising FMMS NPs based on Fe/Mn bimetallic MOFs and developed in this study could release metal ions and MTO into the tumour microenvironment to synergistically induce ferroptosis and ICD to occur, providing a promising new synergistic therapeutic strategy for refractory malignant tumours such as those of colorectal cancer.

The MOFs (FM NPs) were synthesized according to the literature method.[7] The MIL-101 NPs were washed three times with ethanol and distilled water, respectively, and then the Mn element was introducted into MIL-101 by subjecting to a citric acid reduction in the presence of $KMnO_4$ to obtain FM NPs. Subsequently, MTO was loaded into the FM NPs by simply stirring them together to obtain FMM NPs. By adjusting the feed ratio of FM NPs to MTO, FMM NPs with different MTO

[a] College of Basic Medical Sciences, the Medical Basic Research Innovation Centre of Airway Disease in North China, Key Laboratory of Pathobiology, Ministry of Education, Jilin University, Changchun, 130021, China.
E-mail: xucaina@jlu.edu.cn
[b] Department of Oral and Maxillofacial Surgery, School and Hospital of Stomatology, Jilin University, Changchun, 130021, China
[c] Department of Neurology and Neuroscience Centre, First Hospital of Jilin University, Changchun, 130021, China. E-mail: drliuchang@jlu.edu.cn

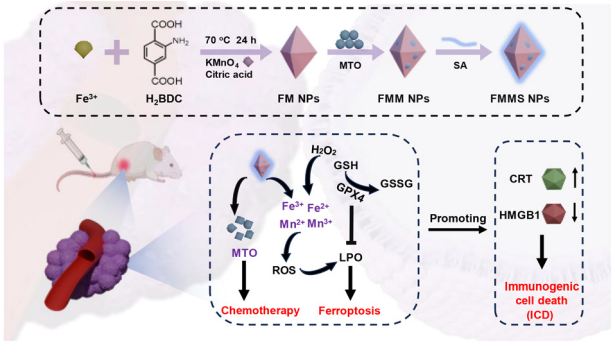

Fig. 1 Schematic representation of the synthesis of FMMS nanoparticles (NPs) and schematic diagram of the mechanism of their use in cancer treatment, achieved *via* chemotherapy, ferroptosis and ICD.

loading amounts could be prepared. The results showed that the drug loading was best when the ratio of FM NPs to MTO was 4 : 1.5, and the MTO encapsulation efficiency was about 26% as measured using a UV-Vis spectrophotometer (Table S1). Finally, the MOF structure was stabilized by loading SA molecules onto the MOF surface to obtain the final products, denoted as FMMS NPs.

Scanning electron microscopy (SEM) images (Fig. 2A and Fig. S1) of FMMS NPs showed a uniform rhombus morphology with dimensions of 211.0 ± 4.2 nm. We also used SEM to examine the morphology of FM NPs and found no significant changes between the morphologies before and after being loaded with the drug (Fig. S2). The zeta potential of FM NPs was −16.1 ± 3.7 mV. After stirring the FM NPs with MTO (zeta potential = −22.4 ± 9.0 mV) to form FMM NPs, the zeta potential was measured to −23.3 ± 1.3 mV, which indicated that MTO had successfully become encapsulated by the MOFs. After modifying the FMM NPs with SA to form FMMS NPs, the zeta potential changed again, to −28.0 ± 1.3 mV, attributed to the introduction of SA -OH groups, and confirming that the surface of FMM NPs had been successfully coated with SA (Fig. 2B). Having negative charges on the surfaces of nanoparticles has been shown to promote the stability and biocompatibility of the nanoparticles in blood circulation.[8] A Brunauer–Emmett–Teller (BET) analysis showed a specific surface area of 204.02 $m^2\ g^{-1}$ for FMMS NPs, lower than that for FM NPs (374.99 $m^2\ g^{-1}$), which also demonstrated that MTO was successfully loaded into the pores of FM NPs and that SA effectively modified FMM NPs (Fig. 2C). X-ray photoelectron spectroscopy (XPS) demonstrated that FMMS NPs were mainly composed of Fe, Mn, N, and O (Fig. S3A). The fine spectrum in its Mn region (Fig. S3B) showed binding energy peaks at 641.5 eV (Mn $2p_{3/2}$) and 652.9 eV (Mn $2p_{1/2}$), corresponding to Mn^{3+}, as well as peaks at 642.9 eV (Mn $2p_{3/2}$) and 654.2 eV (Mn $2p_{1/2}$), corresponding to Mn^{4+}.[9] Similarly, the presence of Fe^{3+} (Fig. S3C) was confirmed by peaks at 721.4 eV (Fe $2p_{3/2}$) and 726.0 eV (Fe $2p_{1/2}$), and the presence of Fe^{2+} was verified by peaks at 710.7 eV (Fe $2p_{3/2}$) and 724.3 eV (Fe $2p_{1/2}$).[10] In addition, peaks were observed at 399.7 eV and 401.3 eV, corresponding to $-NH_2$ of H_2BDC and C–N of MTO, respectively (Fig. S3D).[11] The O 1s region of the spectrum (Fig. S3E) showed peaks at 532.7 eV and 529.8 eV, corresponding to, respectively, the C=O and –OH groups in MTO. And a peak was seen at 531.3 eV, attributed to the –COOH in H_2BDC.[12] These XPS results further confirmed the successful loading of MTO.

As shown in Fig. 2D, the amount of MTO released from FMMS NPs was significantly higher under lower pH conditions. This result indicated that FMMS NPs exhibited pH-responsive drug release properties in the acidic microenvironment of tumours, with this feature beneficial for enhancing the targeted delivery of anti-tumour drugs *in vivo* and for reducing the burst effect under normal physiological conditions.

Since MB is used as an indicator for detecting ·OH generation, various concentrations of FMMS NPs were incubated with MB for 30 min, and absorbance spectra (Fig. 2E) were acquired of each of these mixtures. The absorbance of MB decreased with increasing concentration of FMMS NPs, confirming the ability of FMMS NPs to degrade MB, and reflecting their ability to generate ROS. In addition, we found that GSH, an intracellular antioxidant that protects cells from damage caused by ROS,[13] could be effectively consumed by FMMS NPs. Specifically, the DTNB method was used to detect the GSH content based on its characteristic absorption peak at a wavelength of 412 nm.[14] Here, the absorbance of GSH decreased with increasing concentration of FMMS NPs (Fig. 2F).

As shown in Fig. 3A, the intensity of RhB red fluorescence in CT26 cells was observed to increase with increasing time of incubation with FMMS NPs, demonstrating that FMMS NPs were effectively internalized by CT26 cells in a time-dependent manner, which underlies their significant anti-tumor effects. Inspired by the excellent cellular uptake properties of FMMS NPs, MTT assays were performed on CT26 cells to determine the cytotoxicity levels of FMMS NPs under different conditions. And in Fig. 3B, compared with FM NPs, FMM NPs loaded with MTO exhibited significantly higher tumor cell cytotoxicity. Live/dead cell staining pictures result showed the FMMS NPs group having exhibited the strongest anti-tumor effect (Fig. 3C).

Notably, FMMS NPs exhibited cytotoxicity superior to that exhibited by FMM NPs, likely due to the enhanced dispersibility

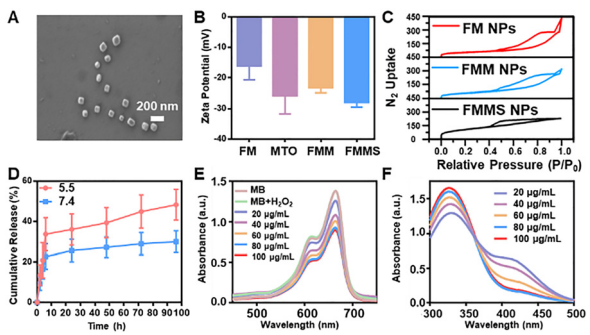

Fig. 2 (A) SEM image of FMMS NPs. (B) Zeta potentials of FM NPs, MTO, FMM NPs, and FMMS NPs (n = 3). (C) Nitrogen absorption curves for FM NPs, FMM NPs, and FMMS NPs. (D) Cumulative releases of MTO from FMMS NPs under indicated pH conditions (n = 3). (E) Absorbance spectra of MB with indicated concentrations of FMMS NPs. (F) GSH consumption and GSSG generation of FMMS NPs.

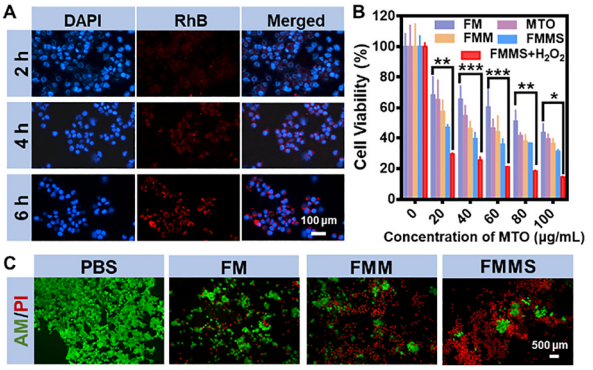

Fig. 3 (A) Fluorescence images of CT26 cells after they were incubated with FMMS NPs for the indicated durations. (B) Viability levels of cells after they were incubated with indicated nanoparticles or drugs at indicated concentrations for 24 h (n = 3). (C) Photographs of live/dead cell staining of CT26 cells under the indicated conditions. Statistical significance was set as follows: *$p < 0.05$, **$p < 0.01$, ***$p < 0.001$, ****$p < 0.0001$.

of SA-loaded particles, which in turn enhanced their biological efficacy. Furthermore, the MTT assay was used to examine the compatibility of FM NPs, MTO, FMM NPs, and FMMS NPs with NIH3T3 cells and L929 cells. The results showed that at a concentration of 40 μg mL^{-1}, FMMS NPs did not cause significant damage to NIH3T3 cells and L929 cells (Fig. S4 and S5), demonstrating their excellent biosafety.

Wound healing assays are a simple and effective method to study cell migration *in vitro*, mimicking to some extent the process *in vivo*.[15] We investigated the effect of FMMS NPs on the migration of CT26 cells using a wound healing assay (Fig. S6A). Compared with the three groups treated with PBS, FM NPs, and FMM NPs, respectively, that treated with FMMS NPs exhibited a significantly lower healing rate, demonstrating their effective inhibition of CT26 cell migration. Furthermore, a colony formation assay revealed that the number of cell colonies formed in the group treated with FMMS NPs was significantly lower than in the other groups, indicating that FMMS NPs significantly inhibited CT26 cell proliferation (Fig. S6B). Comparative wound healing assays using L929 cells showed that the same nanoparticles exhibited no significant inhibitory effect on L929 cell migration (Fig. S7).

We also found that cells that had been incubated with FMMS NPs for 4 h then showed significantly enhanced red fluorescence (Fig. S8), indicating that FMMS NPs could effectively release Fe^{2+} and have it accumulate in the cells.

The DCFH-DA method and flow cytometry were used to detect intracellular ROS levels. The green fluorescence intensity of CT26 cells in the group treated with FMMS NPs was significantly higher than that in the control group (Fig. S9A–C), confirming that FMMS NPs could induce a large amount of ROS generation by relying on metal ion components. Further immunofluorescence and western blot analysis of GPX4 expression showed that the GPX4 protein level in the group treated with FMMS NPs was significantly downregulated (Fig. S10A–C), which was speculated to be related to the strong GSH-depletion ability of FMMS NPs, thereby leading to GPX4 inactivation.

One of the important features of ferroptosis is lipid peroxidation.[16] Also, one of the natural end products of lipid peroxidation is MDA, which indicates the level of LPO in the cells,[17] and so to confirm the occurrence of lipid peroxidation, we measured the amount of MDA. Cells treated with FMMS NPs exhibited higher MDA levels than did controls (Fig. S11), which indicated that FMMS NPs could generate ROS and trigger the inactivation of GPX4, leading to lipid peroxidation and thus ferroptosis. Moreover, ferroptosis is often accompanied by mitochondrial dysfunction, especially a decrease in mitochondrial membrane potential (MMP).[18] JC-1 emits red fluorescence in healthy mitochondria with high mitochondrial membrane potential (MMP), but tends to exhibit green fluorescence in abnormal mitochondria with low MMP. JC-1 probe detection revealed strengthened green fluorescence and weakened red fluorescence in cells treated with FMMS NPs (Fig. S12), indicating decreased MMP activity and severe mitochondrial damage.

To validate the *in vitro* immune activation performed by FM NPs, two representative biomarkers of ICD effects, namely CRT and HMGB1, were evaluated. They were first evaluated using an immunofluorescence assay. The green fluorescence of CRT expression evident on the surface of CT26 cells treated with FM NPs, whereas no green fluorescence was detected in the control group (Fig. S13A). Meanwhile, the green fluorescence of the nuclear protein HMGB1 was significantly attenuated by FM NPs (Fig. S13B), suggesting that ferroptosis mediated a significant ICD effect due to the presence of bimetallic Fe/Mn. MTO can also contribute to ICD. Compared to the group loaded with FM NPs, that loaded with MTO exhibited stronger CRT fluorescence and weaker HMGB1 green fluorescence, suggesting that MTO can also lead to ICD (Fig. S13A and B). Secondly, western blot detection of CRT and HMGB1 expression in CT26 cells was consistent with the immunofluorescence results (Fig. S13C–E).

We also tested the developed products on mice. The animal study was approved and reviewed by the Research Ethics Committee of Jilin University. *In vivo* imaging results showed that Cy5-labeled FMMS NPs intravenously injected into CT26 tumor-bearing mice effectively accumulated in the tumor sites, reaching a peak concentration at 48 h post-injection (Fig. S14), demonstrating excellent tumor targeting. To systematically evaluate the efficacy of the developed system, tumor-bearing mice were randomly divided into five groups and treated with PBS, FM NPs, MTO, FMM NPs, and FMMS NPs, respectively (Fig. 4A). The group treated with FMMS NPs exhibited the strongest inhibitory effect on both tumor volume and mass (Fig. 4B–D). The group treated with FM NPs exhibited some tumor growth inhibition, likely related to ferroptosis and its induced ICD effect. The superior efficacy of FMMS NPs was attributed to the synergistic mechanisms of chemotherapy, ferroptosis, and ICD. Furthermore, TUNEL and Ki-67 staining revealed that FMMS NPs significantly promoted tumor cell apoptosis and inhibited proliferation. Immunofluorescence analysis of tumor tissues revealed downregulation of GPX4 expression, increased 4-HNE levels, upregulation of CRT expression, and HMGB1 release in the mice treated with FMMS NPs (Fig. 4E).

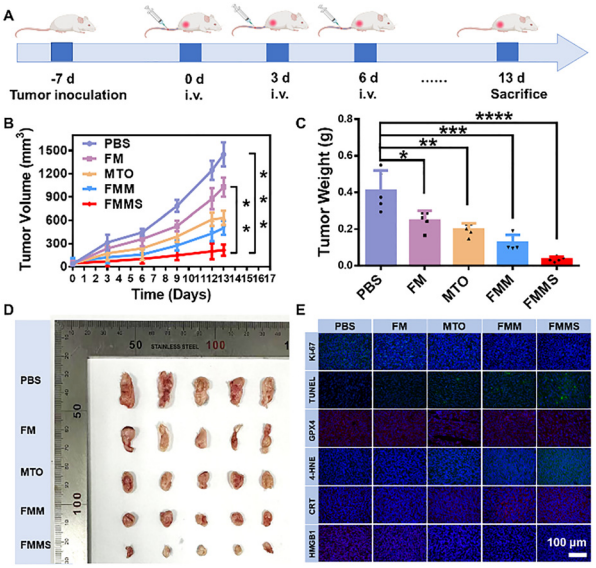

Fig. 4 (A) Schematic diagram of the general treatment regimen for CT26 tumor-bearing mice. (B) Tumor growth curves of CT26 tumor-bearing mice after they were intravenously injected with indicated formulations (n = 5). (C) Tumor weights of the mice in the different groups (n = 5). (D) Photographs of samples obtained from the mice at the end of treatment. (E) Immunofluorescence analysis of Ki-67, TUNEL, GPX4, 4-HNE, HMGB1, and CRT levels in tumors harvested from the different groups of mice. Statistical significance was set as follows: *p < 0.05, **p < 0.01, ***p < 0.001, ****p < 0.0001.

We used several approaches to investigate the biosafety of FMMS NPs. The body weight of tumor-bearing mice in each group remained stable during treatment (Fig. S15), suggesting that FMMS NPs had no significant effect on mouse growth. *In vitro* hemolysis experiments showed that the hemolysis rate of FMMS NPs remained low within the concentration range of 20 to 100 μg mL^{-1} (Fig. S16), demonstrating their excellent hemocompatibility and safety for intravenous injection. Further blood biochemical analysis revealed no significant fluctuations in key parameters (Fig. S17–S22). Furthermore, H&E-stained tissue sections of major organs showed no obvious pathological damage (Fig. S23).

In summary, we successfully constructed a novel nano-delivery system (FMMS NPs) based on bimetallic (Fe/Mn) MOFs encapsulated in SA. This system achieved efficient loading of the chemotherapeutic drug MTO and controlled release responsive to the tumor microenvironment. Mechanistic studies revealed that, upon being internalized by tumor cells, FMMS NPs catalyzed H_2O_2 to generate ROS and downregulate GPX4 expression, synergistically inducing ferroptosis. Simultaneously, the loaded MTO exerted a chemotherapeutic effect and, in conjunction with ferroptosis, triggered ICD. *In vitro* and *in vivo* experiments confirmed that this synergistic combination of chemotherapy, ferroptosis, and ICD endowed FMMS NPs with potent anti-tumor activity, and systematic safety assessments demonstrated their excellent biocompatibility.

Siyuan Wang: writing – original draft, data curation. Shichen Zhang: data curation. Xue Jia: data curation. Xinran Yan: data curation. Yixin Tang: data curation. Mujie Kan: writing – review & editing. Chang Liu: writing – review & editing. Caina Xu: writing – review & editing.

The authors thank the Jilin Province Science and Technology Development Program (20230101045JC), and the Fundamental Research Funds for the Central Universities (2025-JCXK-28).

Conflicts of interest

There are no conflicts to declare.

Data availability

The data supporting this article have been included as part of the supplementary information (SI). Supplementary information is available. Supplementary information: additional supporting data, figures, and experimental details. See DOI: https://doi.org/10.1039/d5cc06597f.

References

1 E. Morgan, M. Arnold, A. Gini, V. Lorenzoni, C. J. Cabasag, M. Laversanne, J. Vignat, J. Ferlay, N. Murphy and F. Bray, *Gut*, 2023, **72**, 338–344.
2 M. Zahra, U. B. Zahra, H. Abrahamse and B. P. George, *RSC Adv.*, 2025, **15**, 37833–37855.
3 Y. W. Wei, Z. H. Wang, J. Yang, R. Xu, H. Z. Deng, S. Y. Ma, T. X. Fang, J. Zhang and Q. Shen, *J. Colloid Interface Sci.*, 2022, **606**, 1950–1965.
4 J. H. Li, W. X. Lv, Z. W. Han, Y. K. Li, J. Q. Deng, Y. J. Huang, S. Wan, J. S. Sun and B. Dai, *Adv. Sci.*, 2025, **12**, 2501542.
5 X. Chen, R. Kang, G. Kroemer and D. L. Tang, *Nat. Rev. Clin. Oncol.*, 2021, **18**, 280–296.
6 H. Zhang, J. Lv, Hao Wu, Y. He, M. Li, C. Wu, D. Lv, Y. Liu and H. Yang, *Sci. Adv.*, 2025, **11**(20), eadq3870.
7 C. Wang, X. D. Jia, W. Y. Zhen, M. C. Zhang and X. Jiang, *ACS Biomater. Sci. Eng.*, 2019, **5**, 4435–4441.
8 Z. Z. Feng, G. Chen, M. Zhong, L. Lin, Z. Y. Mai, Y. Tang, G. M. Chen, W. Ma, G. Li, Y. Y. Yang, Z. Q. Yu and M. Yu, *Biomaterials*, 2023, **302**, 122333.
9 L. M. Yu, Z. Mo, X. L. Zhu, J. J. Deng, F. Xu, Y. H. Song, Y. B. She, H. M. Li and H. Xu, *Green Energy Environ.*, 2021, **6**, 538–545.
10 W. F. Li, T. Zhang, L. Lv, Y. X. Chen, W. X. Tang and S. W. Tang, *Colloid Surface A*, 2021, **624**, 126791.
11 L. Guo, Y. X. Tang, L. Wang, R. Zhou, S. Y. Wang, H. Q. Xu, X. Yang, J. Z. Zhang, J. Chen, C. N. Xu, Y. H. Li and H. Y. Tian, *Adv. Funct. Mater.*, 2024, **34**, 2403188.
12 Z. W. You, Z. Wang, K. X. Tian and X. Y. Yao, *J. Environ. Chem. Eng.*, 2023, **11**, 110159.
13 T. Liu, L. Sun, Y. B. Zhang, Y. L. Wang and J. Zheng, *J. Biochem. Mol. Toxicol.*, 2022, **36**, e22942.
14 K. N. Zhang, H. Sun, L. Wei, R. Hu, H. Liu, Y. C. Lai and X. Li, *Spectrochim. Acta A*, 2025, **328**, 125439.
15 Y. M. Ma, X. H. Li, W. K. Hu, M. Y. Ruan, M. Yang, L. Q. Chang, H. R. Gu and C. Z. Hu, *Microsyst. Nanoeng.*, 2025, **11**, 134.
16 C. H. Liu, Z. H. Liu, Z. Dong, S. J. Liu, H. D. Kan and S. P. Zhang, *J. Genet. Genomics*, 2025, **53**, 1071–1081.
17 X. Zhang, L. C. Hou, Z. Guo, G. C. Wang, J. T. Xu, Z. H. Zheng, K. Sun and F. J. Guo, *Cell Death Discovery*, 2023, **9**, 320.
18 W. Chen, B. Wang, S. S. Liang, L. N. Zheng, H. Fang, S. Xu, T. F. Zhang, M. Wang, X. He and W. Y. Feng, *J. Colloid Interface Sci.*, 2025, **680**, 261–273.

